

# Determining the origin of tidal oscillations in the ionospheric transition region with EISCAT radar and global simulation data

Florian Ludwig Günzkofer<sup>1</sup>, Dmitry Pokhotelov<sup>1</sup>, Gunter Stober<sup>2</sup>, Huixin Liu<sup>3</sup>, Han-Li Liu<sup>4</sup>, Mitchell Nicholas J<sup>5</sup>, Anders Tjulin<sup>6</sup>, and Claudia Borries<sup>7</sup>

<sup>1</sup>German Aerospace Center (DLR)

<sup>2</sup>University of Bern

<sup>3</sup>Earth and Planetary Science Department, Kyushu University

<sup>4</sup>National Center for Atmospheric Research, P. O. Box, 3000, Boulder, CO 80307-3000

<sup>5</sup>Department of Electronic & Electrical Engineering, University of Bath,

<sup>6</sup>EISCAT Scientific Association

<sup>7</sup>German Aerospace Center

November 26, 2022

## Abstract

Solar and atmospheric variability influences the ionosphere, causing critical impacts on satellite and ground based infrastructure. Determining the dominant forcing mechanisms for ionosphere variability is important for prediction and mitigation of these threats. However, this is a challenging task due to the complexity of solar-terrestrial coupling processes. At high latitudes, diurnal and semidiurnal variations of temperature and neutral wind velocity can be forced from either below (lower atmosphere waves) or from above (geomagnetic and in-situ solar forcing). We analyse measurements from the incoherent scatter radar (ISR) facility operated by the European Incoherent Scatter Scientific Association (EISCAT). They are complemented by meteor radar data and compared to global circulation models. Experimental and model data both indicate the existence of strong semidiurnal oscillations in a two-band structure at altitudes  $\lesssim 110$  km and  $\gtrsim 130$  km, respectively. Analysis of the phase progressions suggests the upper band to be forced *in situ* while the lower band corresponds to upwards propagating tides from lower atmosphere. These results show that the actual transition of tides in the altitude region between 90 and 130 km is more complex than described so far.



## Abstract

Solar and atmospheric variability influences the ionosphere, causing critical impacts on satellite and ground based infrastructure. Determining the dominant forcing mechanisms for ionosphere variability is important for prediction and mitigation of these threats. However, this is a challenging task due to the complexity of solar-terrestrial coupling processes. At high latitudes, diurnal and semidiurnal variations of temperature and neutral wind velocity can be forced from either below (lower atmosphere waves) or from above (geomagnetic and in-situ solar forcing). We analyse measurements from the incoherent scatter radar (ISR) facility operated by the European Incoherent Scatter Scientific Association (EISCAT). They are complemented by meteor radar data and compared to global circulation models. Experimental and model data both indicate the existence of strong semidiurnal oscillations in a two-band structure at altitudes  $\lesssim 110$  km and  $\gtrsim 130$  km, respectively. Analysis of the phase progressions suggests the upper band to be forced *in situ* while the lower band corresponds to upwards propagating tides from lower atmosphere. These results show that the actual transition of tides in the altitude region between 90 and 130 km is more complex than described so far.

## 1 Introduction

The ionospheric dynamo region marks the transition from a collision dominated plasma below  $\sim 90$  km to a nearly collisionless plasma above  $\sim 150$  km. Across this transition region, ion/electron gyrofrequencies  $\Omega_{i/e}$  are of the same order as collision frequencies  $\nu_{in/en}$ . As a result, Pedersen and Hall conductivities reach their respective maxima, which in turn permits Pedersen and Hall currents perpendicular to the magnetic field. This enables global magnetospheric field-aligned current systems to be closed at these heights. However, dynamic processes in the transition region can be forced either from "above" (global plasma convection, in-situ solar irradiance absorption, auroral precipitation, etc.) or from "below" (upward propagating waves from lower atmosphere). Determining the actual forcing of specific effects in the transition region will help understanding the complex solar-terrestrial coupling processes.

One parameter to quantify the respective impact of atmospheric and solar effects are tidal-like neutral wind oscillations, especially diurnal (24 hour period) and semidiurnal (12 hour period) variations. Upward-propagating atmospheric tides of both periods are mostly forced due to ultraviolet (UV) absorption by stratospheric ozone and infrared (IR) absorption by tropospheric water vapor. The classical tidal theory (Lindzen, 1979; Andrews et al., 1987; Oberheide et al., 2011) suggests the semidiurnal atmospheric tides to dominate at latitudes above  $\sim 45^\circ$ . At high latitudes, the reconnection between the Earth's magnetic field and the interplanetary magnetic field leads to a large-scale plasma convection pattern (see e.g., Kelly, 2009). This causes a predominantly 24h oscillation of zonal and meridional ion velocities which is transferred to the neutral media via ion drag and frictional heating. The transition from dominant 12h to dominant 24h oscillation regimes is observed at  $\sim 115 - 120$  km altitude (Nozawa et al., 2010). However, there have been evidences for non-negligible semidiurnal oscillations as far up as  $\sim 250$  km (R. Schunk & Nagy, 2009; Wu et al., 2017; Lee et al., 2018). Whether these 12h oscillations are signs of atmospheric tides propagating up into the ionosphere F-region or *in situ* generated oscillations remained an open question. Also, there is a general lack of continuous measurements in the region from 120 km to 250 km.

Thus, we employ two well established observation techniques to measure neutral wind velocities across the mesosphere-lower thermosphere region: meteor radars and ISR. While meteor radars are restricted in altitude coverage by meteor trail occurrence, ISR can cover the whole range from the mesopause well into the thermosphere. In this paper, we leverage the co-located Nordic Meteor Radar Network to verify the validity of the ISR measurements from EISCAT. Based on the combined neutral wind data set, we estimated 12h and 24h oscillations, considering that local measurements do not provide information on the zonal wave number to separate migrating (sun-synchronous) and non-

migrating modes from each other. Such information is taken from global model data such as Ground-to-topside model of Atmosphere and Ionosphere for Aeronomy (GAIA) and the Whole Atmosphere Community Climate Model With Thermosphere and Ionosphere Extension - Specified Dynamics (WACCM-X(SD)). The nomenclature of global tidal modes gives information on period (D: diurnal, S: semidiurnal), propagation direction (W: westward, E: eastward) as seen from an observer at a fixed geographic location on Earth and the zonal wavenumber  $k$  (Smith, 2012). While in principle the latter can take any integer value, we will restrict our analysis to  $0 \leq k \leq 3$  since the by far largest amplitudes are expected for the two sun-synchronous, migrating tidal modes DW1 and SW2 (Smith, 2012).

The determination of tidal amplitudes and phases is done using the Adaptive Spectral Filtering (ASF) technique (Stober et al., 2017). Thereby, the neutral wind data in zonal and meridional direction is separately fitted for a mean background wind and several periodic components. Unless otherwise stated, amplitudes in this paper have been averaged over a sliding window of one day length. The ASF has shown to be a robust frequency analysis method for unequally spaced data (spatially and temporal). Due to the fitting of phases, the propagation of non-stationary processes (phase drifts over time) can be estimated similar to holographic analysis (Stober et al., 2020). The robustness of the fitting for short time windows enables a good resolution of the day-to-day variability of amplitudes compared to other methods. The ASF has been successfully extended and applied to fit for global tidal modes (Baumgarten & Stober, 2019; Stober et al., 2020).

The further structure of the paper is as follows. Section 2 presents the experimental setup and outlines the respective methods of neutral wind retrievals. The numerical models used to generate data are briefly introduced in Section 3. Section 4 presents the results from the analysis of measurement data and highlights the most important features, same is done for the model data in Section 5. The comparison of both as well as the interpretation and discussion are given in Section 6 and the paper is concluded in Section 7.

## 2 Instruments

### 2.1 EISCAT UHF ISR

The EISCAT Ultra High Frequency (UHF) radar at Tromsø is a powerful ISR with about 1.5-2 MW peak power on transmission operating at a frequency of 930 MHz. The system employs a dish with 32 m in diameter resulting in a beam width of about  $0.7^\circ$  corresponding to an antenna directive gain of approximately 48.1 dBi.

In this paper, we analyze UHF EISCAT observations collected during a campaign over more than 20 days in September 2005. This data set presents one of the longest continuous ISR measurements ever performed worldwide. More details on the experiment, data gaps, geomagnetic activity and data quality throughout the campaign are presented in Nozawa et al. (2010). Here, we make use of the existing data base. The EISCAT UHF radar in Tromsø ( $69.6^\circ$  N,  $19.2^\circ$  E) (Folkestad et al., 1983) was operated in the beam swinging mode in which the radar rotates back and forth between four different pointing directions (Collis, 1995). The dwell times at the four positions and the rotation times in between result in a total time resolution of  $\sim 6$  min. From the line of sights ion velocities measured at each pointing direction, three dimensional ion velocity vectors can be derived by inverting the radial wind equation. This is done for seven range gates corresponding to altitudes between 96 km and 142 km and one channel at  $\sim 300$  km.

The procedure of calculating E-region neutral wind velocities  $\mathbf{u}$  from ISR measurements was described in Brekke et al. (1973). It assumes a steady ion velocity  $\mathbf{v}_i$  due to an equilibrium of Lorentz and ion-neutral friction force. The direct solution of the *steady state ion mobility equation* can be applied (Rino et al., 1977; Nozawa et al., 2010)

$$\mathbf{u} = \mathbf{v}_i - \frac{\Omega_i}{B\nu_{in}} (\mathbf{E} + \mathbf{v}_i \times \mathbf{B}). \quad (1)$$

124 As magnetic field  $\mathbf{B}$ , the International Geomagnetic Reference Field (IGRF) (Barraclough,  
 125 1988) is employed. The ion gyrofrequency  $\Omega_i$  is calculated from the magnetic field strength  
 126 and the mean ion mass  $m_i = 30.5$  amu. As suggested by Brekke et al. (1973) and demon-  
 127 strated by Nozawa and Brekke (1999); Nozawa et al. (2010), the electric field  $\mathbf{E}$  can be  
 128 calculated at F-region altitudes and assumed to be the same in the E-region. Since  
 129 ion-neutral collisions can be neglected at higher altitudes, the ion velocity is determined  
 130 by  $E \times B$ -drifts. The electric field is calculated as  $\mathbf{E} = -(\mathbf{v}_{i,F} \times \mathbf{B})$ . F-region ion ve-  
 131 locities  $\mathbf{v}_{i,F}$  are derived from the highest altitude channel at  $\sim 300$  km. The electric field  
 132 originating from plasma convection at high latitudes quantifies the solar impact, whereas  
 133 the atmospheric forcing from below strongly depends on the ion-neutral collision frequency  
 134  $\nu_{in}$ , which is altitude dependent reducing the effective coupling strength with increas-  
 135 ing thermospheric altitude. Very often collision frequencies are inferred from a model neu-  
 136 tral atmosphere (e.g., MSIS Hedin, 1991) and a collision model which can be either em-  
 137 pirical (Chapman, 1956) or analytical (R. W. Schunk & Walker, 1973). In this paper,  
 138 we apply the NRLMSISE-00 model (Picone et al., 2002) and the empirical model for ion-  
 139 neutral collision frequencies

$$\nu_{in} = 2.6 \cdot 10^{-9} \cdot n_n [\text{cm}^{-3}] \cdot A^{-1/2} [\text{s}^{-1}] \quad (2)$$

140 described in Chapman (1956); Kelly (2009), with neutral particle density  $n_n$  and  
 141  $A = m_i$  [amu]. However, the accuracy of any collision model at altitudes  $\gtrsim 120$  km  
 142 has to be considered carefully (Nozawa et al., 2010; Williams & Viridi, 1989). A direct  
 143 measurement of the ion-neutral collision frequencies is possible with the current EISCAT  
 144 system due to its multifrequency capability with simultaneous operation of UHF and VHF  
 145 radars (Grassmann, 1993; Nicolls et al., 2014). Unfortunately, there were no multifre-  
 146 quency experiments scheduled during the investigated campaign and the analysis of these  
 147 requires careful additional testing which is beyond the scope of this paper.

## 148 2.2 Meteor radar

149 Meteor radars have become an ubiquitous sensor monitoring winds at the meso-  
 150 sphere and lower thermosphere. These instruments observe small meteoroids, which are  
 151 formed when extraterrestrial particles with a sufficient kinetic energy enter the Earth's  
 152 atmosphere. Small meteoroids can penetrate deep into the atmosphere until they encounter  
 153 a sufficiently dense region. The impinging atmospheric molecules and atoms decelerate  
 154 and heat the particles to such an extent that the meteoric material is vaporized and atoms  
 155 are released from the meteoroid. Due to the collisions with the ambient neutral atmo-  
 156 sphere the released atoms are thermalized and form an ambipolar diffusing plasma trail,  
 157 often called meteor, that is drifted by the neutral winds. Specular meteor radars detect  
 158 most of these trails at altitudes between 70-110 km. For a large enough number of me-  
 159 teor trails, horizontal wind velocities can be measured with an 'all-sky'-fit (Hocking et  
 160 al., 2001). This is usually done with a time resolution of 1h and 2 km altitude bins.

161 In Kiruna (67.9° N, 21.1° E), a meteor radar has been continuously operated since  
 162 1999 and therefore provides measurement for the time of the EISCAT campaign described  
 163 above. Meteor radars have been used for the investigation of various types of waves in  
 164 the upper atmosphere, including atmospheric tides, and provide a well tested measure-  
 165 ment method (Pokhotelov et al., 2018; Stober et al., 2021). Since the derivation of neu-  
 166 tral wind velocities from EISCAT measurements is not as well established, meteor radar  
 167 measurements can be used as a reference at the lower boundary. In this paper, measure-  
 168 ments from EISCAT and the Kiruna meteor radar will be merged to test the validity of  
 169 the procedure described in the previous section. A large offset of ISR and meteor radar

170 data would be clearly visible if present. Also, the total observed altitude range is extended  
 171 significantly downwards.

### 172 3 Models

#### 173 3.1 GAIA

174 The Ground-to-Topside Model of Atmosphere and Ionosphere for Aeronomy (GAIA)  
 175 is a global circulation model (GCM) giving neutral dynamics for all altitudes from the  
 176 ground up to  $\sim 600$  km (Jin et al., 2012). GAIA data has been compared and verified  
 177 with experiment data from numerous different apparatuses for time spans up to several  
 178 decades. The GAIA dataset used for the analysis presented in Section 5 has been pre-  
 179 viously applied for long term investigations in H. Liu et al. (2017) and Stober et al. (2021).  
 180 We summarize the most important features and refer to these publications for more de-  
 181 tailed information.

182 The atmosphere up to  $\sim 30$  km altitude is constrained to the JRA-25/55 reanal-  
 183 ysis (Onogi et al., 2007) using a nudging technique. While the solar irradiance is parametrized  
 184 with the F10.7 index, the geomagnetic activity is set to a constant value. Therefore, the  
 185 cross polar potential is held at 30 kV for all model data, corresponding to a moderate  
 186 geomagnetic activity. The neutral wind components are provided on a grid with a res-  
 187 olution of  $1^\circ$  in latitude and  $2.5^\circ$  in longitude. The altitude resolution is  $1/5$  of the re-  
 188 spective scale height at each altitude. The analysis presented in this paper has been con-  
 189 ducted with preprocessed files giving the data in 10 km altitude bins. The time resolu-  
 190 tion is 0.5 h.

#### 191 3.2 WACCM-X(SD)

192 The Community Earth System Model (CESM) is a combination of models cover-  
 193 ing different parts of the Earth system (Hurrell et al., 2013). The Whole Atmosphere  
 194 Community Climate Model Extension WACCM-X (H.-L. Liu et al., 2018) is the part of  
 195 the CESM describing the atmosphere from the ground up to  $\gtrsim 500$  km. The data pre-  
 196 sented in this paper was generated with a *Special Dynamics* run WACCM-X(SD) (Gasparini  
 197 et al., 2020) and previously used in Stober et al. (2021). Again, we only give a brief overview  
 198 and refer to the mentioned publications.

199 The lower atmosphere is constrained up to  $\sim 50$  km to NASA’s reanalysis MERRA  
 200 (Rienecker et al., 2011). Other than the used GAIA run, WACCM-X(SD) does not set  
 201 a fixed cross polar potential. The polar convection is calculated using the *Heelis* model  
 202 (Heelis et al., 1982) and the geomagnetic activity is therefore parametrized by the Kp  
 203 index. The longitudinal resolution is  $2.5^\circ$  and values are given in 3h intervals. Since the  
 204 model is evaluated on hydrostatic pressure levels, the altitude range extends from 992.5  
 205 hPa near the ground up to  $\sim 4 \cdot 10^{-10}$  hPa. The height resolution above  $\sim 50$  km is  
 206  $1/4$  of the respective scale height. The corresponding geopotential altitudes are given  
 207 for each time and position and range roughly from the ground up to  $\sim 500$  km. In the  
 208 transition region, the geopotential height resolution varies between 1 km and 5 km.

209 The different parametrization of geomagnetic activity in the used GAIA and WACCM-  
 210 X runs are ideal to investigate its influence on neutral winds at different altitudes. How-  
 211 ever, since both models extend to the ground and are restrained to reanalysis of mete-  
 212 orological data (Stober et al., 2021), it is not feasible investigating the impact of atmo-  
 213 spheric forcing in these models.

#### 214 3.3 TIE-GCM

215 The Thermosphere Ionosphere Electrodynamics General Circulation Model (TIE-  
 216 GCM) (Richmond et al., 1992) is a stand alone ionosphere model and also part of the  
 217 Coupled Magnetosphere-Ionosphere-Thermosphere Model (CMIT) (Qian et al., 2014).

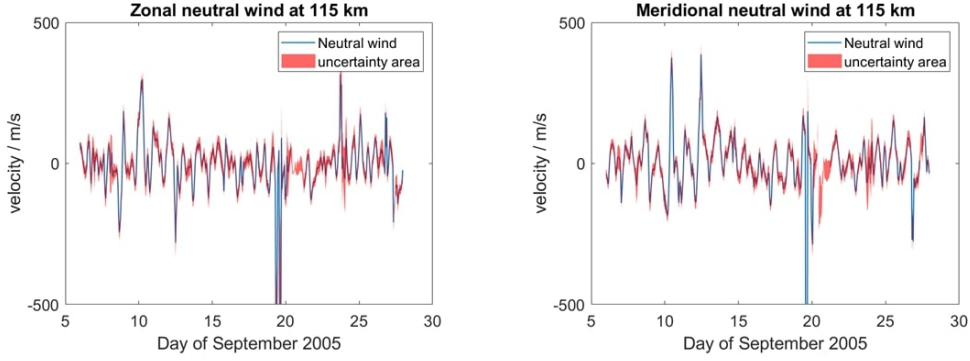


**Figure 1.** Neutral winds at 115 km altitude in zonal (left) and meridional (right) direction. The uncertainty has been determined from the measurement uncertainty by means of Gaussian error propagation.

218 The data presented in this paper was generated from several runs performed with the  
 219 TIE-GCM Model Version 2.0.

220 In contrast to the two models described above, TIE-GCM does not extend down  
 221 to the ground, but implies a lower boundary condition at  $\sim 99$  km altitude. The hor-  
 222 izontal neutral winds and neutral temperatures at the boundary are specified by input  
 223 files. These quantities are calculated from the monthly averaged amplitudes and phases  
 224 of diurnal and semidiurnal tides given by the Global Scale Wave Model (GSWM) (Hagan  
 225 & Forbes, 2002, 2003). Performing separate runs with empirical GSWM tidal input, al-  
 226 ternated values or no tidal input at all allows to assess the impact of atmospheric dy-  
 227 namics and the forcing from below. Same as for WACCM-X, the *Heelis* model is used  
 228 to obtain the cross polar potentials and geomagnetic activity is parametrized according  
 229 to the Heelis parametrization (Heelis et al., 1982). TIE-GCM gives output data on a  $2.5^\circ$   
 230  $\times 2.5^\circ$  grid with a time resolution of 1h. Furthermore, TIE-GCM data is provided on  
 231 logarithmic altitude coordinates (*atmospheric ln pressure coordinate*)  $\ln\left(\frac{p_0}{p}\right)$  for the pres-  
 232 sure  $p$  at a certain altitude. The reference pressure  $p_0 = 5 \cdot 10^{-5}$  hPa corresponds roughly  
 233 to  $\sim 225$  km altitude and the atmospheric ln pressure coordinate ranges from -6.875 to  
 234 7.125 in 0.25 increments. This corresponds to a resolution of 1/4 in scale height units.  
 235 The geopotential altitude ranges from  $\sim 96$  km to  $\sim 590$  km with a resolution that steadily  
 236 increases from  $\sim 2$  km to  $\sim 18$  km with increasing height.

## 237 4 Experiment data

238 This section will give an overview on the results from analysis of experimental data  
 239 with the instruments presented in Section 2. The most important features will be high-  
 240 lighted. Interpretation of these features and comparison to the results from model data  
 241 analysis will be given in Section 6.

### 242 4.1 Neutral wind

243 As described in Section 2.1, three dimensional ion velocity vectors were calculated  
 244 from four line of sight measurements and then used to derive three dimensional neutral  
 245 wind vectors. Figure 1 shows the calculated neutral winds in zonal and meridional di-  
 246 rections for the measurement channel corresponding to 115 km altitude.

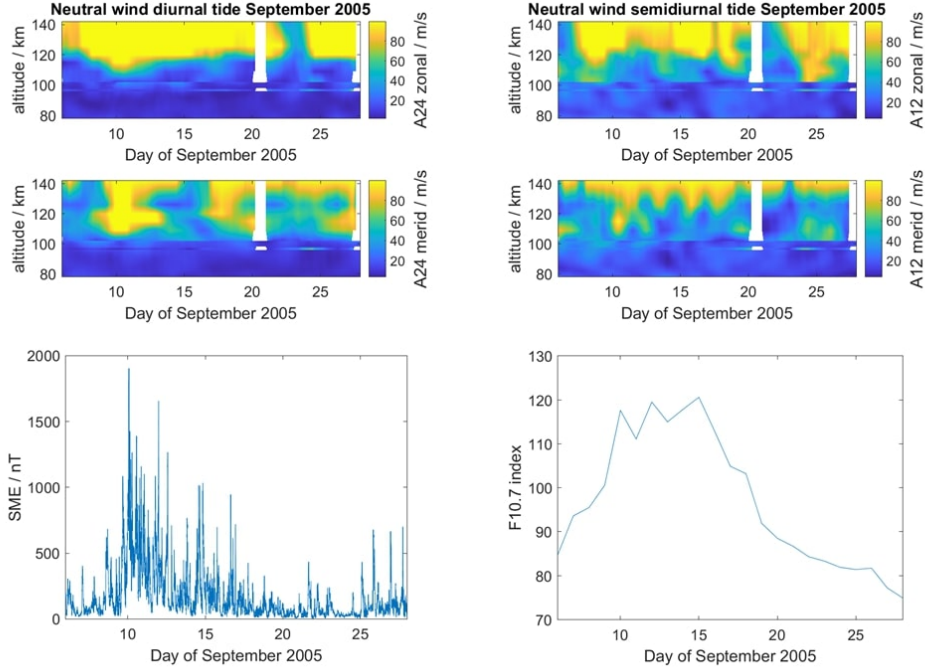


**Figure 2.** The upper row shows the amplitudes of diurnal (left) and semidiurnal (right) oscillations in zonal (top) and meridional (bottom) direction during September 2005. Data from EISCAT and meteor radar are merged together. The lower row shows the variations of geomagnetic activity (magnetic local time subset of the SME index, left) and the solar irradiation (F10.7 index, right) during the measurement time.

247 Error bars shown in Figure 1 are calculated from the ion velocity measurement un-  
 248 certainties which affect the neutral wind values both directly and via the electric field  
 249 calculation. Uncertainties of the ion-neutral collision frequency, which can have a major  
 250 impact (Williams & Virdi, 1989), are not shown. While the relative uncertainties at  
 251 altitudes  $\gtrsim 110$  km are reasonably small ( $\leq 40\%$ ), they tend to increase with decreasing  
 252 altitudes ( $\leq 70\%$ ). The lower electron density results in smaller signal-to-noise ratios  
 253 and consequently to increased statistical uncertainties in the derived ISR parameters.  
 254 Neutral wind velocities calculated from EISCAT measurements at low altitudes should  
 255 therefore be treated carefully when looking at absolute values. The determination of tidal-  
 256 like oscillation amplitudes, however, is still possible with reasonable accuracy compared  
 257 to other altitudes since the ASF technique takes into account uncertainties of the input  
 258 data. The strong outliers at single timepoints (around day 19) and data gaps (around  
 259 day 21) visible in Figure 1, both likely caused by problems with the radar system, can  
 260 also be handled by the ASF method.

261 The diurnal and semidiurnal amplitudes are determined separately for each alti-  
 262 tude level. Figure 2 shows the amplitudes of tidal-like oscillations measured by the Kiruna  
 263 meteor radar ( $80 \text{ km} \leq h \leq 104 \text{ km}$ ) and the EISCAT UHF in Tromsø ( $96 \text{ km} \leq h \leq$   
 264  $142 \text{ km}$ ). To see possible correlations, indices for geomagnetic activity and solar irradi-  
 265 ation during the time of the measurement campaign are also shown in Figure 2. The Su-  
 266 perMAG Auroral Electrojet (SME) index and its subsets in magnetic local time (MLT)  
 267 quantify the geomagnetic activity. A more detailed description will be given in Section  
 268 4.2. The F10.7 index is commonly used to quantify solar irradiation.

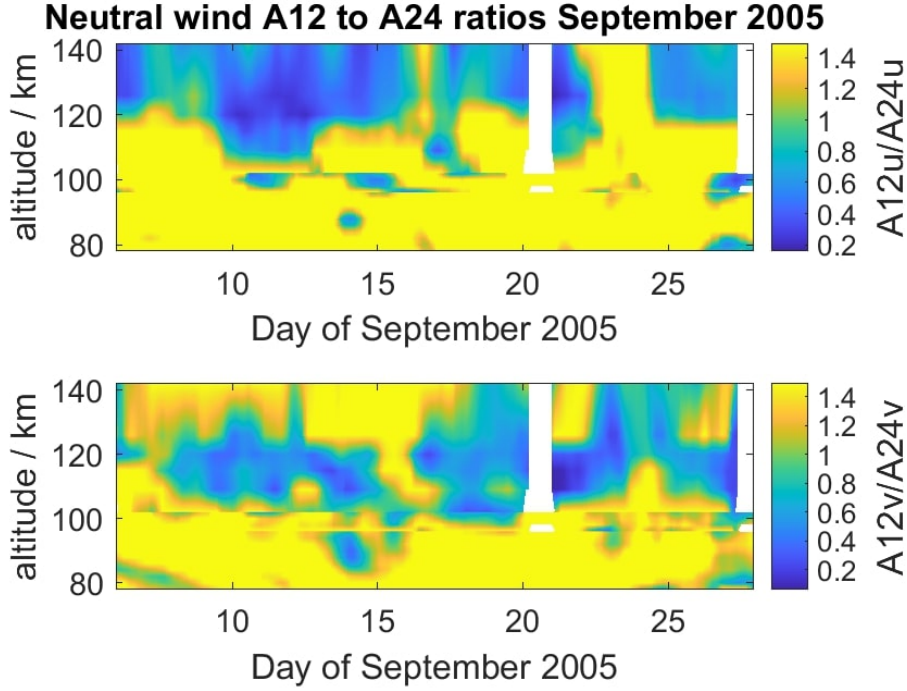


**Figure 3.** Ratio of semidiurnal to diurnal amplitudes shows two-band structure of dominant semidiurnal oscillations.

269 The figure shows the merged amplitudes of both systems and reflects the transi-  
 270 tion altitude between both instruments at about 100 km. Additionally, the graphic in-  
 271 dicated the presence of a data gap around September 21st for the EISCAT observations,  
 272 whereas the meteor radar wind time series remains uninterrupted during the entire peri-  
 273 od. Considering the different geographic locations of both instruments, which are about  
 274 100 km apart from each other, the similarity of the amplitudes in magnitude and variabil-  
 275 ity is remarkable. Some features even seem to extend across the coverage gap (see A12  
 276 meridional, around September 15th). This strongly reinforces the validity of the neutral  
 277 wind calculation method summarized in Section 2.1. Both oscillations show an increas-  
 278 ing amplitude with altitude due to decreasing atmospheric density. Especially the diurn-  
 279 al oscillations are difficult to recognize at 120 km. The variability of diurnal and semi-  
 280 diurnal oscillations can now be compared and investigated concerning a different forcing  
 281 mechanism.

282 The next step is the determination of the dominant tidal mode at each time and  
 283 altitude. Therefore, the amplitude ratio of semidiurnal and diurnal oscillations is cal-  
 284 culated and shown in Figure 3.

285 The ratio of zonal amplitudes  $A_{12u}/A_{24u}$  in the upper plot of Figure 3 corresponds  
 286 very much to what is expected from the tidal theory (Lindzen, 1979). Semidiurnal vari-  
 287 ations are predominant up to altitudes of  $\sim 110$ – $120$  km. Above that, most of the time  
 288 diurnal oscillations exhibit larger amplitudes. Meridional tidal amplitudes, however,  
 289 indicate distinct differences and, thus, points out that this tidal component governed by  
 290 additional more complicated physical processes. While the transition from predominant  
 291 semidiurnal to diurnal tide also takes place at and around 110 km altitude, there is an  
 292 upper band of strong semidiurnal oscillations especially during the first half of Septem-  
 293 ber. This apparent weakening of the upper SW2 band around equinox is an important  
 294 feature since atmospherically forced SW2 tides have been shown to undergo such an au-

295 tumn transition (Pedatella et al., 2021). Whether this upper band is generated *in situ*  
 296 or forced by some atmospheric tidal mode that propagates unusually far up remains to  
 297 be investigated in more detail.

298 Assuming *in situ* generation being correlated to geomagnetic activity, one can ap-  
 299 ply a geomagnetic activity filter and thereby visualize how oscillations behave differently  
 300 by setting thresholds to define high and low activity periods.

## 301 4.2 Geomagnetic activity filter

302 There are various indices quantifying the geomagnetic activity at different latitudes  
 303 and sometimes also longitudes. At high latitudes, the Auroral Electrojet (AE) index is  
 304 probably the most commonly used, measuring the strength of east- and westwards di-  
 305 rected currents in the auroral zone. However, the AE index uses a set of stations spread  
 306 across all longitudes. Since the measurements presented in this paper only cover a lo-  
 307 cal region around  $\sim 20^\circ$  E longitude, it is more appropriate to use an index that also  
 308 includes local subsets.

309 The SuperMAG Auroral Electrojet (SME) index (Newell & Gjerloev, 2011) is cal-  
 310 culated from magnetometer data taken by all stations of the SuperMAG network in a  
 311 latitudinal range from  $40^\circ$  N to  $80^\circ$  N. Additionally to a global index value, the SME in-  
 312 dex is given in 24 local sub-channels, each covering one hour of magnetic local time (MLT)  
 313 (Newell & Gjerloev, 2014). Knowing the magnetic local time at Tromsø (MLT = UTC  
 314 + 2.5), it is possible to bin the data time intervals corresponding to the appropriate MLT  
 315 channel for each observation and, thereby, generating a local SME index.

316 A superposed epoch analysis (SEA) (Singh & Badruddin, 2006) is performed on  
 317 a set of local SME indices for each of the 30 days during September 2005. To filter out  
 318 high activity periods, a local SME index filter threshold  $0.0 \leq T_{SME} \leq 1.0$  is defined.  
 319 For instance  $T_{SME} = 0.9$  means that for each time of day, the ten percent highest ac-  
 320 tivity observations are not included in the analysis. Figure 4 shows the diurnal and semi-  
 321 diurnal amplitudes in the meridional neutral wind determined for three different datasets  
 322 with different  $T_{SME}$  values.

323 It should be noted here again, that while the amplitudes are fitted on the data with  
 324 a temporal resolution of 6 min, the amplitudes are averaged using a one day sliding win-  
 325 dow. Therefore, gaps in the presented data will only occur if the SME index is consis-  
 326 tently above the defined threshold for at least a full day. Shorter high activity periods  
 327 will not be considered for the ASF fitting, but an amplitude value is given for these times  
 328 due to the averaging. The possibility of ASF being applied on a dataset with notable  
 329 gaps is central at this point.

330 The upper row of Figure 4 shows the unfiltered ( $T_{SME} = 1.0$ ) meridional ampli-  
 331 tudes. Both amplitudes maximise for higher altitudes. There are periods, most notably  
 332 at and shortly after day 10, where large diurnal amplitudes seem to be present at lower  
 333 altitudes. A similar effect, but weaker, is observed for semidiurnal amplitudes at the same  
 334 time. The analysis on the filtered datasets for  $T_{SME} = 0.9$  and  $T_{SME} = 0.8$  indicates  
 335 that such enhancements of the diurnal amplitudes at lower altitudes appears to be con-  
 336 nected to periods of consistently high geomagnetic activity. Shorter time intervals of high  
 337 activity exhibit a much weaker effect since the amplitudes of the filtered data changes  
 338 only slightly compared to the unfiltered observations during the rest of the month. The  
 339 increase of diurnal amplitude for stronger geomagnetic activity could be expected since  
 340 the convection electric fields are directly connected to auroral currents. The fact that  
 341 a similar correlation is observed for the semidiurnal tidal amplitudes suggests, however,  
 342 that this tidal mode also depends on the geomagnetic activity. This would mean that  
 343 semidiurnal oscillations at high altitudes are not the result of upwards propagating at-  
 344 mospheric tides. The upper altitude band seen in Figure 3 would rather be *in situ* gen-  
 345 erated according to this.

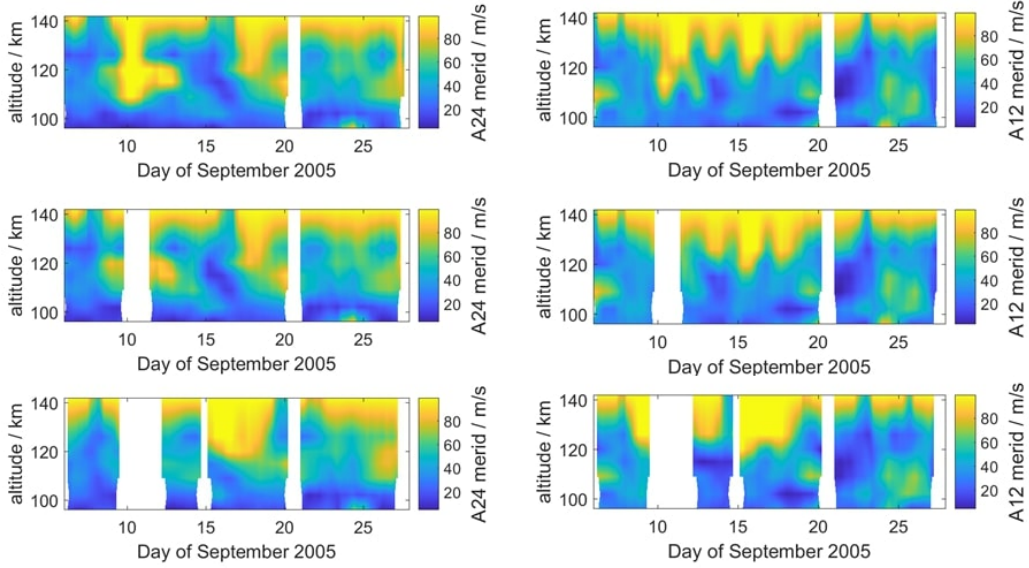


**Figure 4.** Geomagnetic impact on meridional amplitudes of diurnal (left) and semidiurnal (right) oscillations shown by comparison of amplitudes with local SME index thresholds  $T_{SME} = [1.0; 0.9; 0.8]$  (from the top). For both diurnal and semidiurnal oscillations, strong amplitudes reaching down to 120 km can be associated with high geomagnetic activity.

346 If the semidiurnal variations are indeed connected to the same convection electric  
 347 fields as the diurnal oscillations, the 12h amplitude should be visible in the ion veloc-  
 348 ities at higher altitudes as well.

### 349 4.3 High altitude ion velocities

350 F-region neutral winds are inferred from the ion velocity observations of EISCAT.  
 351 The ion velocities at  $\sim 300$  km altitude permit to estimate the convection electric field  
 352 required in Equation 1. Furthermore, these high altitude ion velocities can now be di-  
 353 rectly investigated for periodicities. Diurnal and semidiurnal amplitudes are shown in  
 354 Figure 5.

355 The diurnal amplitudes exhibit a pronounced peak at and shortly after day 10, which  
 356 occurs coincidentally with the increased geomagnetic activity. A second, smaller peak,  
 357 at day 15 can also be attributed to geomagnetic activity. At the magnetic latitude MLAT  
 358 67 in Tromsø, the stronger zonal variations fit the two cell convection pattern very well,  
 359 whereas closer to the geomagnetic pole the meridional component becomes dominant (Wu  
 360 et al., 2017). The semidiurnal oscillations exhibit a very similar pattern with distinct peaks  
 361 during high activity periods. Furthermore, the diurnal and semidiurnal wind variations  
 362 are stronger in the zonal component than in the meridional. As expected, the semidi-  
 363 urnal amplitudes are weaker compared to the diurnal amplitudes. However, the 12h vari-  
 364 ations shown in Figure 5 are notably higher than a higher harmonic of 24h oscillation.  
 365 This leads to the conclusion that polar convection might force semidiurnal oscillations.  
 366 Possible reasons for this are discussed in Section 6.

367 To obtain more information about the spatial shape of this semidiurnal tidal-like  
 368 oscillations and its origin, global model data is analysed.

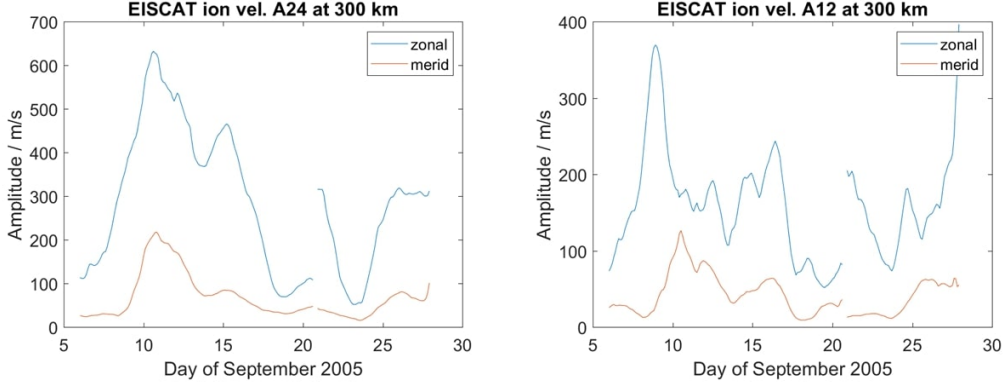


**Figure 5.** Diurnal (left) and semidiurnal (right) amplitudes in the ion velocities from the F-region altitude channel measured with EISCAT.

## 5 Model data

This section will give an overview on the results from analysis of global simulation data with the models presented in Section 3. The most important features will be highlighted. Interpretation of these features and comparison to the results from measurement data analysis will be given in Section 6.

### 5.1 Neutral wind

GCM models provide neutral wind velocities on a global longitude and latitude grid. The data is analyzed in the range from day 200 to 320 (July 19th to November 16th) of the year 2005. The plots in this Section are restricted to the days of the EISCAT measurement campaign to allow a direct comparison of the dynamics over these days. The neutral wind velocities are analysed at a single latitude corresponding to Tromsø for all datasets. Furthermore, the GCM longitudinal resolution is the same in all models with  $2.5^\circ$ .

As described in Section 1, the ASF here fits not only for the time period of neutral wind oscillations but also for zonal wave numbers  $0 \leq k \leq 3$ . To compare the model data with the measurements, the perspective of a local observer needs to be taken into account. The resultant amplitudes of the combined migrating and non-migrating modes were extracted at  $20^\circ$  E longitude to ensure that a comparison with the observations is meaningful. As expected, the clearly dominating tidal-like modes for both diurnal and semidiurnal oscillations are the sun-synchronous modes DW1 and SW2. Therefore, we only present the obtained amplitudes for these modes.

To investigate the impact of different forcings from below, model runs with different lower boundaries are compared.

#### 5.1.1 Impact of geomagnetic activity (GAIA and WACCM-X(SD))

As described in Section 3, the GAIA applies a constant cross polar potential corresponding to a low geomagnetic activity. The impact of geomagnetic activity will be determined by comparison to the WACCM-X(SD) run. However, since polar convection is not completely switched off in the GAIA, the impact of the convection pattern can only be determined by comparing data from both models and data from the mid-latitudes, which should be almost not affected by the geomagnetic activity.

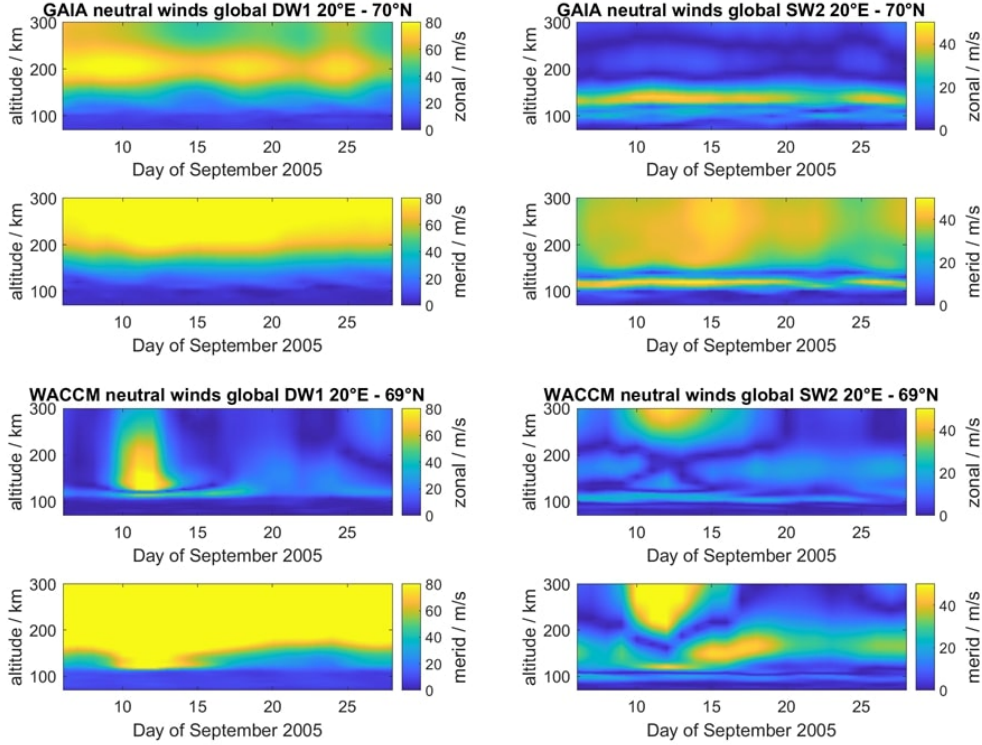


**Figure 6.** Comparison of GAIA (top) and WACCM-X(SD) (bottom) amplitudes of the DW1 (left) and SW2 (right) tidal modes at high latitudes ( $70^\circ$  N).

399 Figure 6 shows the amplitudes of DW1 and SW2 obtained from GAIA and WACCM-  
 400 X(SD) data evaluated at the Tromsø geographical position.

401 To ensure comparability between data from model runs with different forcing or  
 402 evaluated at different latitudes, the colour scale is kept the same for all view graphs. Within  
 403 the expected deviations due to different handling of geomagnetic activity, the models show  
 404 similar tidal-like behaviour:

405 The diurnal oscillations exhibit large amplitudes in the meridional component at  
 406 high altitudes in both models during the selected time interval. This indicates that oscil-  
 407 lations forced by plasma convection in the F-region have a larger impact on the tran-  
 408 sition region processes for higher geomagnetic activity.

409 The semidiurnal amplitudes indicate a pronounced maximum band at or slightly  
 410 above  $\sim 100$  km altitude in both models and for the zonal and meridional direction. Ac-  
 411 cording to classical tidal theory, this is associated with upward propagating atmospheric  
 412 tides. The amplitude of vertically propagating tides is supposed to show an exponen-  
 413 tial growth with increasing altitude. However, at the lower transition region the wave  
 414 energy starts to be dissipated due to the ion drag (Smith, 2012). Additionally, both sim-  
 415 ulations show a multi-band structure of strong semidiurnal amplitudes. GAIA shows two  
 416 bands in both zonal and meridional direction with the upper band extending down to  
 417  $\sim 130 - 160$  km. This upper band is clearly more influential in meridional direction,  
 418 linking it to the convection pattern, and seems to undergo a transition process around  
 419 the autumn equinox. This autumn transition can also be found in the WACCM-X(SD)  
 420 data. This run even exhibits a third band at altitudes  $\gtrsim 200$  km. Here, we will focus  
 421 on the second band which is taken to correspond to the upper band in the GAIA run.  
 422 This second band reflects strong semidiurnal oscillations, which appear to be inhibited

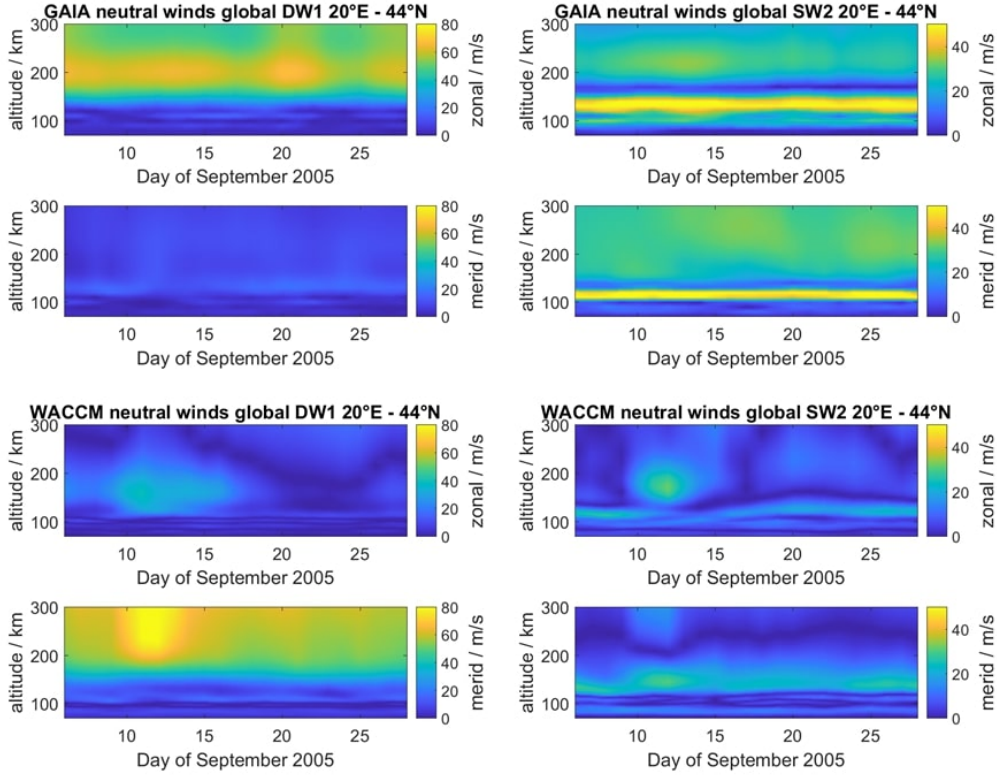


**Figure 7.** Comparison of GAIA (top) and WACCM-X(SD) (bottom) amplitudes of the DW1 (left) and SW2 (right) tidal modes at mid latitudes ( $44^\circ$  N).

or not excited in zonal direction, presumably also due to the larger extension of the convection pattern as discussed before.

In conclusion, it can be said that both model runs agree in various important and unexpected features, mostly the multi-band structure of the SW2 tidal-like mode. Though there are distinct differences, these seem to be mostly caused by the different parametrization of geomagnetic activity. A forcing of both DW1 and SW2 oscillations by polar plasma convection seem to provide a reasonable explanation of the observed results.

To investigate this conclusion even further, one can look at the neutral wind data from the same model runs at mid-latitudes where the polar convection should have no influence. Figure 7 shows the exact same tidal-like modes as Figure 6 but at  $44^\circ$  northern latitude.

The diurnal amplitudes are decreased in both models for both directions at all altitudes. This monotonous decrease strongly indicates polar convection to be a major source of neutral wind oscillations. It can also be seen that the decrease is stronger in meridional direction where the amplitudes went down to almost negligible magnitude in GAIA and significantly reduced compared to the strong amplitudes in WACCM-X(SD). While also smaller, the zonal amplitudes underwent less of a reduction going from high- to mid-latitudes. The meridional DW1 oscillations are definitely connected to high latitude effects. For zonal oscillations there seems to be at least one other significant effect which has nearly equal strength at polar and mid-latitudes.

The SW2 oscillation maximum at  $\sim 100$  km associated with upward propagating tides is also visible at lower latitudes, providing confidence to our previous interpretation. The upper band is missing in the WACCM-X(SD) data. This is contrary to GAIA,

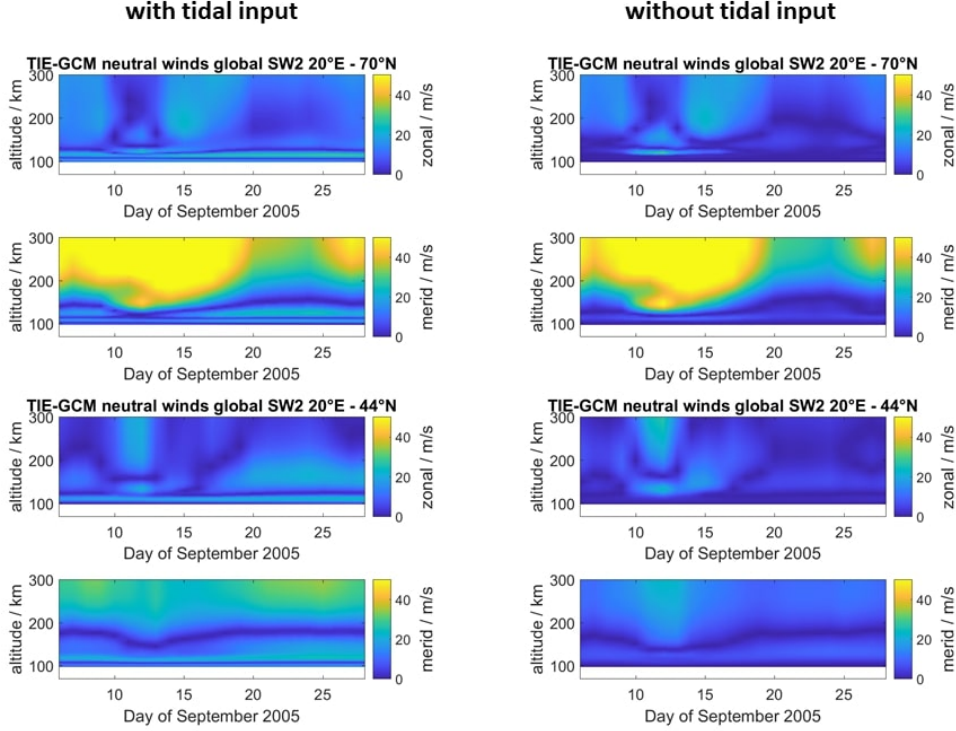


**Figure 8.** Amplitudes of SW2 tidal-like oscillation from the TIE-GCM model at high (up) and mid-latitudes (bottom). Presented are two separate runs with realistic (left) and zero (right) atmospheric tidal input.

446 which indicates an upper band of strong semidiurnal oscillations. The transition of the  
 447 SW2 oscillations observed around autumn equinox seems to be reversed at mid-latitudes  
 448 with the upper band tending to gain intensity afterwards. This transition and the fact  
 449 that the upper SW2 band does not completely vanish at mid-latitudes indicates that it  
 450 might not be forced only by polar plasma convection but rather due to an interplay of  
 451 several processes. Different wave modes forced by these processes interfere. If the forc-  
 452 ing changes, this can lead to a change from constructive to destructive interference. Dif-  
 453 ferent interference of the wave modes could explain the sudden transitions observed around  
 454 equinox.

455 **5.1.2 Impact of atmospheric forcing (TIE-GCM)**

456 Comprehensive models such as GAIA and WACCM-X involve complex processes,  
 457 which have to be parametrized posing challenges to conduct and investigate more iso-  
 458 lated processes. TIE-GCM offers the possibility to investigate the ionosphere and ther-  
 459 mosphere by applying a well-defined lower boundary condition describing the middle at-  
 460 mospheric forcing. Figure 8 shows the results of two different model runs, one performed  
 461 using an empirical input for tidal oscillations at 99 km and one with tidal amplitudes  
 462 set to zero at the boundary. The dominance of sun-synchronous tidal-like modes and the  
 463 behaviour of DW1 oscillations are similar as found in other models. Therefore, further  
 464 investigations are restricted to SW2 oscillations from these model runs.

465 Additionally to different atmospheric boundary conditions, different latitudes are  
 466 considered as well. At high latitudes, the TIE-GCM run with empirical GSWM tidal forc-

ing exhibits a SW2 amplitude structure that resembles the tidal fields very similar to the ones shown in Figure 6 from GAIA and WACCM-X(SD). This run indicates a two band structure accompanied by a transition of the upper band around the autumn equinox. Though, the lower band is notably weaker than in the other models suggesting that the tidal amplitudes are underestimated for the lower boundary. This is confirmed when comparing the amplitudes of TIE-GCM initialized with a zero tidal activity at the lower boundary. In this model run, the lower band mostly vanishes, whereas the upper band appears to be not affected, which also excludes an atmospheric forcing as origin of the upper SW2 band structure. It should be noted, that propagating tides forced by EUV absorption above the lower boundary are still present in TIE-GCM. At mid-latitude, we obtain a similar picture as already found in Figure 7, showing a notably reduced SW2 amplitude at high altitudes and a nearly unaffected amplitude at lower altitudes. Most interestingly here, even the high altitude SW2 oscillations are still visible and seem to be forced by the propagating tides from the middle atmosphere, since they vanish in the run with artificially zero tidal forcing at the lower boundary. Prompting the same conclusion of the upper SW2 band being linked to the polar plasma convection, this also brings new insight regarding the transition around equinox. Indeed, there seem to be several processes that drive SW2-like oscillations and the observed autumn transition seems to be caused by their interaction.

## 5.2 Phase progression analysis

Phase progression analysis permits to distinguish between propagating tidal modes and *in situ* generated evanescent modes. The time of maximum should be steadily shifted with altitude for an upwards propagating oscillation, showing as a swift change of phase. Semidiurnal oscillations observed in EISCAT data below 120 km have been identified to correspond to upward propagating atmospheric tides (Nozawa et al., 2010). Furthermore, the model data is used in this paper to extend the altitude coverage well into the F-layer at mid- and polar-latitudes. Figure 9 shows the time of maximum of the semidiurnal oscillations in the meridional winds extracted from GAIA and WACCM-X(SD). To emphasize the autumn transition seen in the oscillation amplitudes, the whole range of model data from day 200 to day 320 is shown here.

Both models show a steady phase progression at low altitudes and nearly constant phase at higher altitudes. The boundary between progressing and constant phase is notably higher up in GAIA which is related to the fixed low geomagnetic activity in the model. For both models, the boundaries are found at similar altitudes as the upper SW2 band in Figure 6. This clearly reinforces the conclusion that the lower SW2 band is caused by upwards propagating atmospheric tides and the upper SW2 band is *in situ* forced. The mentioned boundary between progressing and constant phase additionally allows to mark the transition from dominant solar to terrestrial atmospheric dynamical forcing. The sudden transition around equinox (DOY 265) is also visible in the phases, especially from GAIA data at high latitudes. This suggests a strongly increased propagation of atmospheric tides as main cause for the transition. WACCM-X(SD) uses much stronger geomagnetic activity which counteracts the upwards propagation of tides. This might explain why the transition is more pronounced in GAIA data. At mid-latitudes, both models show a steady change of the phase boundary. The reversed transition of the upper SW2 band seen in Figure 7 cannot be explained from the shown phase progression. However, phase progression analysis is a helpful technique to quantify the respective influence of geomagnetic and atmospheric forces and to identify the altitude where the dominant processes change.

## 5.3 High altitude ion velocities

Since the high altitude ion velocity oscillations are measured in EISCAT at 300 km altitude, the reliability of the model data at high altitudes can be partially verified. Con-

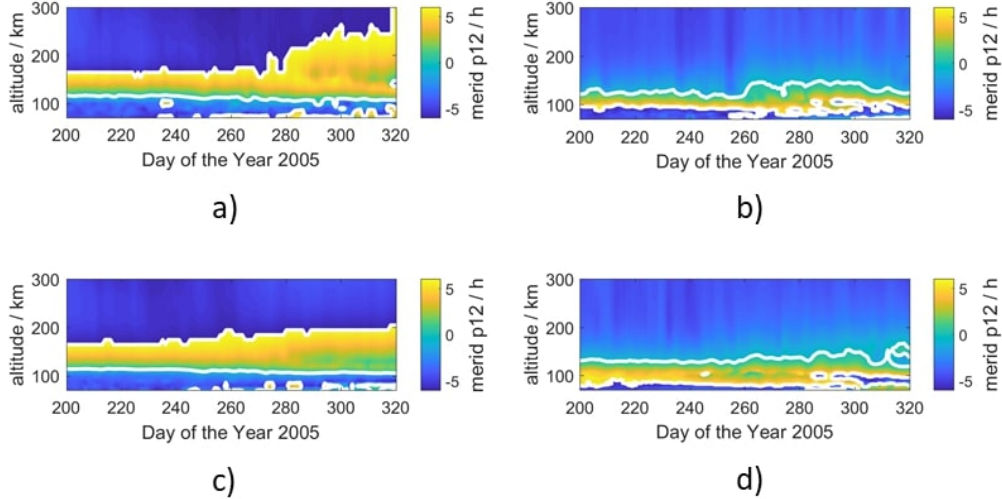


**Figure 9.** Phase progression of the SW2 mode from GAIA (a and c) and WACCM-X(SD) (b and d) at high latitudes (a and b) and mid-latitudes (c and d). Both models give a nearly constant phase at the altitudes of the upper band, indicating an *in situ* generation of this band.

518 sidering that GAIA uses a constant cross-polar potential, it is expected that plasma con-  
 519 vection ion velocities should indicate increased discrepancies compared to the ISR obser-  
 520 vations. WACCM-X(SD) and TIE-GCM include the Kp index to parametrize geo-  
 521 magnetic activity and therefore should achieve a better agreement in the ion velocities  
 522 resembling the measurements. Figure 10 shows diurnal and semidiurnal oscillation am-  
 523 plitudes of the ion velocity at 300 km altitude from GAIA, WACCM-X(SD) and TIE-  
 524 GCM.

525 It can be seen that the diurnal oscillation amplitudes are dominant and indicate  
 526 reasonable agreement for TIE-GCM and WACCM-X(SD), which was already found for  
 527 the geomagnetic activity. Semidiurnal oscillations also have significant amplitudes and  
 528 tentatively also correspond to the geomagnetic activity. It can be concluded that semid-  
 529 iurnal oscillations at high altitudes are forced by the same plasma convection as diurn-  
 530 al oscillations. GAIA ion velocity amplitudes are similar to WACCM-X(SD) and TIE-  
 531 GCM amplitudes at low activity times and show little variability. The ion velocity os-  
 532 cillations of WACCM-X(SD) and TIE-GCM are highly similar in amplitudes and dynam-  
 533 ics.

## 534 6 Interpretation of results from measurements and models

535 The first part of this study evaluated the validity of both EISCAT measurements  
 536 in comparison to the model fields from GAIA and WACCM-X(SD). The neutral wind  
 537 computation method applied to EISCAT data was verified with meteor radar measure-  
 538 ments for the overlapping altitude region. From the combined data set, combined neu-  
 539 tral wind measurements from  $\sim 80$ –140 km altitude were derived. Since meteor radars  
 540 have proven to be a highly reliable and worldwide used technique (see Section 2.2 and  
 541 references there within), the good agreement between EISCAT and meteor radar am-  
 542 plitudes suggests a good reliability of both neutral wind data products. The most im-  
 543 portant feature found from the analysis of the EISCAT measurements was an upper band  
 544 of unexpectedly strong semidiurnal oscillations. Comparison with the results from three  
 545 separate ionosphere GCM models confirmed a two band structure of 12h modulations

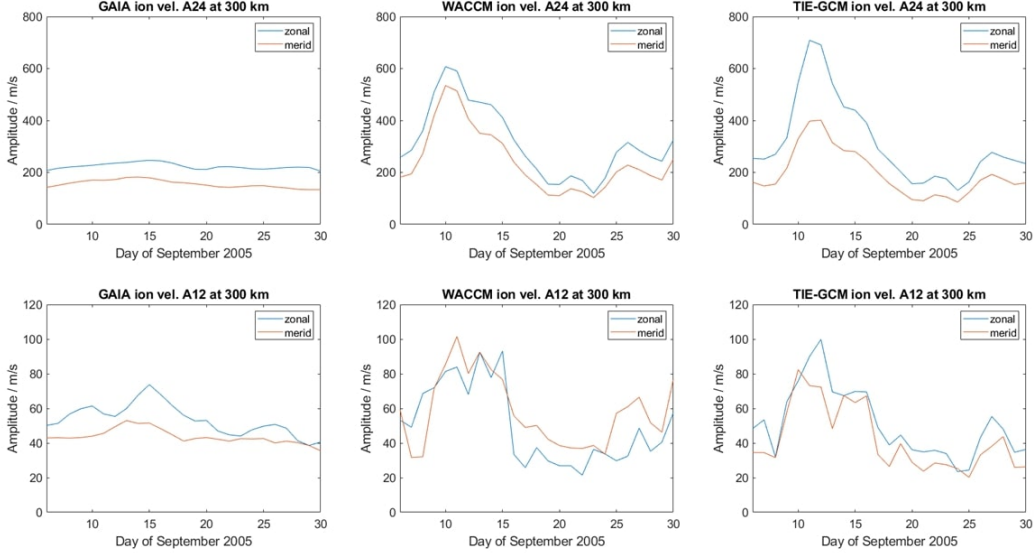


**Figure 10.** Diurnal (top) and semidiurnal (bottom) high altitude ion velocity amplitudes from GAIA, WACCM-X(SD) and TIE-GCM (left to right).

546 in the ionosphere. However, the three models all give different amplitudes and indicate  
 547 altitudinal differences of the transition regions between the 12h oscillation bands. We  
 548 attribute this to different handling of geomagnetic activity and the cross-polar poten-  
 549 tial, which affects the plasma convection pattern and strength within the polar cap. The  
 550 observed lowest altitude of the upper semidiurnal oscillation band of  $\sim 120$  km – 140  
 551 km is well within the possible range given by WACCM-X(SD) and TIE-GCM. These use  
 552 a more realistic approximation of geomagnetic activity than the GAIA. The application  
 553 of a geomagnetic activity filter on the EISCAT data revealed that at high altitudes both  
 554 diurnal and semidiurnal oscillations are forced by geomagnetic activity. For high activ-  
 555 ity, strong oscillation amplitudes can reach down to low altitudes. This is supported by  
 556 large amplitudes even down to low altitudes in those models which do not assume a gen-  
 557 erally low geomagnetic activity. The comparison with mid-latitudes also in global mod-  
 558 els further reinforces the measurement finding by suggesting the polar plasma convec-  
 559 tion as origin of the upper semidiurnal oscillation band found with EISCAT. Additional  
 560 to the apparent linkage to geomagnetic activity, the upper semidiurnal band seems to  
 561 be nearly independent from atmospheric forcing. Two TIE-GCM runs with and with-  
 562 out atmospheric boundary at  $\sim 99$  km show that while the lower 12h band vanishes when  
 563 a net zero tidal atmospheric forcing is applied, however, the upper semidiurnal oscilla-  
 564 tion region remains unchanged. This renders atmospheric forcing of the observed two  
 565 band structure unlikely. However, the transition of the upper SW2 band around equinox  
 566 as seen in all three models as well as EISCAT (also previously reported by Nozawa et  
 567 al. (2010)) is very similar to what is expected for the lower SW2 band (Pedatella et al.,  
 568 2021). In fact, the GAIA and WACCM-X(SD) runs clearly show transitions of the lower  
 569 SW2 band at similar times as the upper one. This underlines a potential *in situ* forc-  
 570 ing of high altitude SW2 oscillations, a possible connection to atmospheric dynamics re-  
 571 mains with the observed autumn transition. The conclusion of forcing from above and  
 572 below each being responsible for one of the observed regions is confirmed by the phase  
 573 progression analysis. The phases of semidiurnal oscillations in the investigated model runs  
 574 show a transition from phase propagation at low altitudes, corresponding to vertically  
 575 propagating tidal modes, and a constant phase at high altitudes suggesting an *in situ*  
 576 generation. Phase progression analysis also reveals a defined altitude at which the dom-

577 inant impact changes from atmospheric to geomagnetic forcing, marking a very impor-  
 578 tant point for ionospheric dynamic. Again, different models show diverse transition al-  
 579 titudes due to different implementations of the geomagnetic activity. Furthermore, we  
 580 report another feature that was found by comparing high altitude ion velocities from EIS-  
 581 CAT, WACCM-X(SD) and TIE-GCM, which reflect in the general morphology and also  
 582 the amplitudes. However, the relative amplitudes between zonal and meridional ion ve-  
 583 locities reflect distinct differences, which are not entirely understood. This might be con-  
 584 nected with different shapes and sizes of the polar convection pattern and consequently  
 585 different positioning of the evaluated grid point within this pattern. GAIA and WACCM-  
 586 X(SD) apply different approaches on how the geomagnetic activity is implemented in the  
 587 models resulting in different plasma convection patterns. In addition, the deviation of  
 588 the *Heelis* model from the actual polar convection is not yet fully understood and re-  
 589 quires further investigations that are beyond the present paper.

## 590 7 Conclusion

591 It has been shown that it is possible to perform continuous and combined obser-  
 592 vations of neutral wind velocities with meteor radars and incoherent scatter radars. Such  
 593 simultaneous observations are of major importance when studying the coupling of at-  
 594 mospheric phenomena into the ionosphere. Another methodological improvement in this  
 595 paper is the first use of the ASF technique on EISCAT measurements. This technique  
 596 permits to resolve the day-to-day variability of unevenly sampled time series and an im-  
 597 proved handling of the measurement uncertainties which are highly relevant in the ISR  
 598 method. The thereby enabled larger altitude range revealed a previously not reported  
 599 two band structure of strong semidiurnal oscillations. Using several global ionosphere  
 600 models, we confirmed the measured two band structure and showed that both diurnal  
 601 and semidiurnal tidal-like oscillations are sun-synchronous (DW1 and SW2). Phase pro-  
 602 gression analysis and different atmospheric boundaries settings showed that the lower  
 603 SW2 band is presumably a upwards propagating atmospheric tide. Tidal-like oscillations  
 604 higher up are *in situ* forced and related to geomagnetic activity as shown in measure-  
 605 ments. Comparing models at high and mid-latitudes suggest the origin of this forcing  
 606 to be the polar plasma convection. The autumn transition of the high altitude SW2 os-  
 607 cillation, seen both in measurements and model, resembles a previously reported autumn  
 608 transition of SW2 oscillations (Pedatella et al., 2021). This suggests the existence of more  
 609 than one forcing process. The exact mechanism behind this remains to be identified and  
 610 studied in future investigations. The same goes for the suspected differences of size and  
 611 shape of the plasma convection pattern in different models and reality which might be  
 612 responsible for discrepancies in the relation of zonal and meridional dynamics.

## 613 Open Research

614 The model and measurement data used in this paper as well as the input files for  
 615 the conducted TIE-GCM runs can be found under doi:10.5281/zenodo.6343418 (Günzkofer  
 616 et al., 2022). In case of further questions about the data and the used analysis software  
 617 please contact the corresponding author. The analysis software will be shared upon re-  
 618 quest.

## 619 Acknowledgments

620 The authors would like to acknowledge the following data sources:  
 621 EISCAT is an international association supported by research organisations in China (CRIRP),  
 622 Finland (SA), Japan (NIPR and ISEE), Norway (NFR), Sweden (VR), and the United  
 623 Kingdom (UKRI).  
 624 We gratefully acknowledge the SuperMAG collaborators ([http://supermag.jhuapl.edu/info/?](http://supermag.jhuapl.edu/info/?page=acknowledgement)  
 625 [page=acknowledgement](http://supermag.jhuapl.edu/info/?page=acknowledgement)) for providing the SME index.

For this study, a dataset from the Ground-to-topside model of Atmosphere and Ionosphere for Aeronomy (GAIA) project carried out by the National Institute of Information and Communications Technology (NICT), Kyushu University, and Seikei University was used. The WACCM-X model has been developed at NCAR (see <https://www2.hao.ucar.edu/modeling/waccm-x>).

The TIEGCM and related Thermosphere-Ionosphere models have been developed by the “Atmosphere Ionosphere Magnetosphere” (AIM) Section of the High Altitude Observatory (HAO) at NCAR (see <http://www.hao.ucar.edu/modeling/tgcm>). The TIEGCM data was generated on the ‘Kratos’ High-Performance Data Analysis Cluster (HPDA).

## References

- Andrews, D. G., Holton, J. R., & Leovy, C. B. (1987). *Middle atmosphere dynamics*.
- Barracough, D. R. (1988, April). IAGA Division I Working Group 1: International Geomagnetic Reference Field revision 1987. *Geophysical Journal International*, *93*(1), 187-189. doi: 10.1111/j.1365-246X.1988.tb01397.x
- Baumgarten, K., & Stober, G. (2019). On the evaluation of the phase relation between temperature and wind tides based on ground-based measurements and reanalysis data in the middle atmosphere. *Annales Geophysicae*, *37*(4), 581–602. Retrieved from <https://angeo.copernicus.org/articles/37/581/2019/> doi: 10.5194/angeo-37-581-2019
- Brekke, A., Doupnik, J. R., & Banks, P. M. (1973, December). A preliminary study of the neutral wind in the auroral E region. , *78*(34), 8235-8250. doi: 10.1029/JA078i034p08235
- Chapman, S. (1956, August). The electrical conductivity of the ionosphere: A review. *Il Nuovo Cimento*, *4*(S4), 1385-1412. doi: 10.1007/BF02746310
- Collis, P. N. (1995, August). EISCAT data base for ionospheric modelling: F-region and topside ionosphere. *Advances in Space Research*, *16*(1), 37-46. doi: 10.1016/0273-1177(95)00096-W
- Folkestad, K., Hagfors, T., & Westerlund, S. (1983, December). EISCAT: An updated description of technical characteristics and operational capabilities. *Radio Science*, *18*(6), 867-879. doi: 10.1029/RS018i006p00867
- Gasparini, F., Liu, H., & McInerney, J. (2020, May). Preliminary Evidence of Madden-Julian Oscillation Effects on Ultrafast Tropical Waves in the Thermosphere. *Journal of Geophysical Research (Space Physics)*, *125*(5), e27649. doi: 10.1029/2019JA027649
- Grassmann, V. (1993, April). An incoherent scatter experiment for the measurement of particle collisions. *Journal of Atmospheric and Terrestrial Physics*, *55*(4-5), 573-576. doi: 10.1016/0021-9169(93)90006-K
- Günzkofer, F., Pokhotelov, D., Stober, G., Liu, H., Liu, H., Mitchell, N. J., ... Borries, C. (2022, March). *Determining the origin of tidal oscillations in the ionospheric transition region with EISCAT radar and global simulation data*. Zenodo. ([Dataset]) doi: 10.5281/zenodo.6343418
- Hagan, M. E., & Forbes, J. M. (2002, December). Migrating and nonmigrating diurnal tides in the middle and upper atmosphere excited by tropospheric latent heat release. *Journal of Geophysical Research (Atmospheres)*, *107*(D24), 4754. doi: 10.1029/2001JD001236
- Hagan, M. E., & Forbes, J. M. (2003, February). Migrating and nonmigrating semidiurnal tides in the upper atmosphere excited by tropospheric latent heat release. *Journal of Geophysical Research (Space Physics)*, *108*(A2), 1062. doi: 10.1029/2002JA009466
- Hedin, A. E. (1991, February). Extension of the MSIS thermosphere model into the middle and lower atmosphere. , *96*(A2), 1159-1172. doi: 10.1029/90JA02125
- Heelis, R. A., Lowell, J. K., & Spiro, R. W. (1982, August). A model of the

- 679 high-latitude ionospheric convection pattern. , *87*(A8), 6339-6345. doi:  
680 10.1029/JA087iA08p06339
- 681 Hocking, W. K., Fuller, B., & Vandeppeer, B. (2001, January). Real-time determina-  
682 tion of meteor-related parameters utilizing modern digital technology. *Journal*  
683 *of Atmospheric and Solar-Terrestrial Physics*, *63*(2-3), 155-169. doi: 10.1016/  
684 S1364-6826(00)00138-3
- 685 Hurrell, J. W., Holland, M. M., Gent, P. R., Ghan, S., Kay, J. E., Kushner, P. J.,  
686 ... Marshall, S. (2013, September). The Community Earth System Model: A  
687 Framework for Collaborative Research. *Bulletin of the American Meteorological*  
688 *Society*, *94*(9), 1339-1360. doi: 10.1175/BAMS-D-12-00121.1
- 689 Jin, H., Miyoshi, Y., Pancheva, D., Mukhtarov, P., Fujiwara, H., & Shinagawa,  
690 H. (2012, October). Response of migrating tides to the stratospheric sud-  
691 den warming in 2009 and their effects on the ionosphere studied by a whole  
692 atmosphere-ionosphere model GAIA with COSMIC and TIMED/SABER  
693 observations. *Journal of Geophysical Research (Space Physics)*, *117*(A10),  
694 A10323. doi: 10.1029/2012JA017650
- 695 Kelly, M. C. (2009). *The Earth's Ionosphere: Plasma Physics and Electrodynamics,*  
696 *Second Edition.*
- 697 Lee, W., Kim, Y. H., Lee, C., & Wu, Q. (2018, December). First Comparison of  
698 Mesospheric Winds Measured with a Fabry-Perot Interferometer and Meteor  
699 Radar at the King Sejong Station (62.2°S, 58.8°W). *Journal of Astronomy and*  
700 *Space Sciences*, *35*, 235-242. doi: 10.5140/JASS.2018.35.4.235
- 701 Lindzen, R. S. (1979, January). Atmospheric Tides. *Annual Review of Earth and*  
702 *Planetary Sciences*, *7*, 199. doi: 10.1146/annurev.earth.07.050179.001215
- 703 Liu, H., Sun, Y.-Y., Miyoshi, Y., & Jin, H. (2017, May). ENSO effects on MLT  
704 diurnal tides: A 21 year reanalysis data-driven GAIA model simulation. *Jour-*  
705 *nal of Geophysical Research (Space Physics)*, *122*(5), 5539-5549. doi: 10.1002/  
706 2017JA024011
- 707 Liu, H.-L., Bardeen, C. G., Foster, B. T., Lauritzen, P., Liu, J., Lu, G., ... Wang,  
708 W. (2018, February). Development and Validation of the Whole Atmosphere  
709 Community Climate Model With Thermosphere and Ionosphere Extension  
710 (WACCM-X 2.0). *Journal of Advances in Modeling Earth Systems*, *10*(2),  
711 381-402. doi: 10.1002/2017MS001232
- 712 Newell, P. T., & Gjerloev, J. W. (2011, December). Evaluation of SuperMAG  
713 auroral electrojet indices as indicators of substorms and auroral power.  
714 *Journal of Geophysical Research (Space Physics)*, *116*(A12), A12211. doi:  
715 10.1029/2011JA016779
- 716 Newell, P. T., & Gjerloev, J. W. (2014, December). Local geomagnetic indices  
717 and the prediction of auroral power. *Journal of Geophysical Research (Space*  
718 *Physics)*, *119*(12), 9790-9803. doi: 10.1002/2014JA020524
- 719 Nicolls, M. J., Bahcivan, H., Häggström, I., & Rietveld, M. (2014, December). Di-  
720 rect measurement of lower thermospheric neutral density using multifrequency  
721 incoherent scattering. , *41*(23), 8147-8154. doi: 10.1002/2014GL062204
- 722 Nozawa, S., & Brekke, A. (1999, January). Studies of the auroral E region  
723 neutral wind through a solar cycle: Quiet days. , *104*(A1), 45-66. doi:  
724 10.1029/1998JA900013
- 725 Nozawa, S., Ogawa, Y., Oyama, S., Fujiwara, H., Tsuda, T., Brekke, A., ... Fu-  
726 jii, R. (2010, August). Tidal waves in the polar lower thermosphere ob-  
727 served using the EISCAT long run data set obtained in September 2005.  
728 *Journal of Geophysical Research (Space Physics)*, *115*(A8), A08312. doi:  
729 10.1029/2009JA015237
- 730 Oberheide, J., Forbes, J. M., Zhang, X., & Bruinsma, S. L. (2011, November). Cli-  
731 matology of upward propagating diurnal and semidiurnal tides in the thermo-  
732 sphere. *Journal of Geophysical Research (Space Physics)*, *116*(A11), A11306.  
733 doi: 10.1029/2011JA016784

- 734 Onogi, K., Tsutsui, J., Koide, H., Sakamoto, M., Kobayashi, S., Hatsushika, H., ...  
735 Taira, R. (2007, January). The JRA-25 Reanalysis. *Journal of the Meteorolog-*  
736 *ical Society of Japan*, *85*(3), 369-432. doi: 10.2151/jmsj.85.369
- 737 Pedatella, N. M., Liu, H. L., Conte, J. F., Chau, J. L., Hall, C., Jacobi, C., ... Tsut-  
738 sumi, M. (2021, February). Migrating Semidiurnal Tide During the September  
739 Equinox Transition in the Northern Hemisphere. *Journal of Geophysical Re-*  
740 *search (Atmospheres)*, *126*(3), e33822. doi: 10.1029/2020JD033822
- 741 Picone, J. M., Hedin, A. E., Drob, D. P., & Aikin, A. C. (2002, December).  
742 NRLMSISE-00 empirical model of the atmosphere: Statistical comparisons and  
743 scientific issues. *Journal of Geophysical Research (Space Physics)*, *107*(A12),  
744 1468. doi: 10.1029/2002JA009430
- 745 Pokhotelov, D., Becker, E., Stober, G., & Chau, J. L. (2018, June). Seasonal  
746 variability of atmospheric tides in the mesosphere and lower thermosphere:  
747 meteor radar data and simulations. *Annales Geophysicae*, *36*(3), 825-830. doi:  
748 10.5194/angeo-36-825-2018
- 749 Qian, L., Burns, A. G., Emery, B. A., Foster, B., Lu, G., Maute, A., ... Wang,  
750 W. (2014). The near tie-gcm: A community model of the coupled thermo-  
751 sphere/ionosphere system, in *Modeling the Ionosphere-Thermosphere System*,  
752 geophysical monograph series, vol. 201. In (p. 73-83). American Geophysical  
753 Union. doi: 10.1002/9781118704417.ch7
- 754 Richmond, A. D., Ridley, E. C., & Roble, R. G. (1992, March). A thermo-  
755 sphere/ionosphere general circulation model with coupled electrodynamics.  
756 , *19*(6), 601-604. doi: 10.1029/92GL00401
- 757 Rienecker, M. M., Suarez, M. J., Gelaro, R., Todling, R., Bacmeister, J., Liu, E., ...  
758 Woollen, J. (2011, July). MERRA: NASA's Modern-Era Retrospective Analy-  
759 sis for Research and Applications. *Journal of Climate*, *24*(14), 3624-3648. doi:  
760 10.1175/JCLI-D-11-00015.1
- 761 Rino, C. L., Brekke, A., & Baron, M. J. (1977, June). High-resolution auroral zone  
762 E region neutral wind and current measurements by incoherent scatter radar. ,  
763 *82*(16), 2295. doi: 10.1029/JA082i016p02295
- 764 Schunk, R., & Nagy, A. (2009). *Ionospheres: Physics, Plasma Physics, and Chem-*  
765 *istry*. doi: 10.1017/CBO9780511635342
- 766 Schunk, R. W., & Walker, J. C. G. (1973, November). Theoretical ion densities in  
767 the lower ionosphere. , *21*(11), 1875-1896. doi: 10.1016/0032-0633(73)90118-9
- 768 Singh, Y. P., & Badruddin. (2006, April). Statistical considerations in su-  
769 perposed epoch analysis and its applications in space research. *Jour-*  
770 *nal of Atmospheric and Solar-Terrestrial Physics*, *68*(7), 803-813. doi:  
771 10.1016/j.jastp.2006.01.007
- 772 Smith, A. K. (2012, November). Global Dynamics of the MLT. *Surveys in Geo-*  
773 *physics*, *33*(6), 1177-1230. doi: 10.1007/s10712-012-9196-9
- 774 Stober, G., Baumgarten, K., McCormack, J. P., Brown, P., & Czarnecki, J. (2020,  
775 October). Comparative study between ground-based observations and  
776 NAVGEM-HA analysis data in the mesosphere and lower thermosphere  
777 region. *Atmospheric Chemistry & Physics*, *20*(20), 11979-12010. doi:  
778 10.5194/acp-20-11979-2020
- 779 Stober, G., Kuchar, A., Pokhotelov, D., Liu, H., Liu, H.-L., Schmidt, H., ...  
780 Mitchell, N. (2021, September). Interhemispheric differences of mesosphere-  
781 lower thermosphere winds and tides investigated from three whole-atmosphere  
782 models and meteor radar observations. *Atmospheric Chemistry & Physics*,  
783 *21*(18), 13855-13902. doi: 10.5194/acp-21-13855-2021
- 784 Stober, G., Matthias, V., Jacobi, C., Wilhelm, S., Höffner, J., & Chau, J. L. (2017,  
785 June). Exceptionally strong summer-like zonal wind reversal in the upper  
786 mesosphere during winter 2015/16. *Annales Geophysicae*, *35*(3), 711-720. doi:  
787 10.5194/angeo-35-711-2017
- 788 Williams, P. J. S., & Viridi, T. S. (1989, January). EISCAT observations of tidal

789 modes in the lower thermosphere. *Journal of Atmospheric and Terrestrial*  
790 *Physics*, 51(7), 569-577. doi: 10.1016/0021-9169(89)90055-X  
791 Wu, Q., Jee, G., Lee, C., Kim, J.-H., Kim, Y. H., Ward, W., & Varney, R. H. (2017,  
792 January). First simultaneous multistation observations of the polar cap ther-  
793 mospheric winds. *Journal of Geophysical Research (Space Physics)*, 122(1),  
794 907-915. doi: 10.1002/2016JA023560